nature photonics

SUPPLEMENTARY INFORMATION
https://doi.org/10.1038/s41566-019-0516-1

In the format provided by the authors and unedited.

Topological strong-field physics on sub-laser-cycle timescale

R. E. F. Silva[1,2,8]*, Á. Jiménez-Galán[1,8]*, B. Amorim[3,4], O. Smirnova[1,5] and M. Ivanov[1,6,7]

[1]Max-Born-Institute, Berlin, Germany. [2]Department of Theoretical Condensed Matter Physics, Universidad Autónoma de Madrid, Madrid, Spain. [3]CeFEMA, Instituto Superior Técnico, Universidade de Lisboa, Lisbon, Portugal. [4]Department of Physics, Center of Physics, and QuantaLab, University of Minho, Campus of Gualtar, Braga, Portugal. [5]Technische Universität Berlin, Ernst-Ruska-Gebäude, Berlin, Germany. [6]Department of Physics, Humboldt University, Berlin, Germany. [7]Blackett Laboratory, Imperial College London, South Kensington Campus, London, UK. [8]These authors contributed equally: R. E. F. Silva, Á. Jiménez-Galán. *e-mail: ruiefdasilva@gmail.com; jimenez@mbi-berlin.de

Supplementary information: Topological strong field physics on sub-laser cycle timescale.

R. E. F. Silva[1,2], Á. Jiménez-Galán[1], B. Amorim[3,4], O. Smirnova[1,5], and M. Ivanov[1,6,7]

[1] *Max-Born-Institute, Max-Born Straße 2A, D-12489 Berlin, Germany.*
[2] *Department of Theoretical Condensed Matter Physics, Universidad Autónoma de Madrid, E-28049 Madrid, Spain.*
[3] *CeFEMA, Instituto Superior Técnico, Universidade de Lisboa, Av. Rovisco Pais, 1049-001 Lisboa, Portugal.*
[4] *Department of Physics, Center of Physics, and QuantaLab, University of Minho, Campus of Gualtar, 4710-057, Braga, Portugal.*
[5] *Technische Universität Berlin, Ernst-Ruska-Gebäude, Hardenbergstraße 36A, 10623 Berlin, Germany.*
[6] *Department of Physics, Humboldt University, Newtonstraße 15, D-12489 Berlin, Germany.*
[7] *Blackett Laboratory, Imperial College London, South Kensington Campus, SW7 2AZ London, United Kingdom.*

Supplementary note 1

In the main text we have stated that the helicity of the high harmonics from Chern insulators changes upon the topological phase transition, but the first harmonic does not. We define the helicity as

$$e = \frac{I_{\circlearrowright} - I_{\circlearrowleft}}{I_{\circlearrowright} + I_{\circlearrowleft}}, \tag{1}$$

where $I_{\circlearrowright}$ ($I_{\circlearrowleft}$) is the harmonic intensity rotating clockwise (anticlockwise), which can be measured using a polarizer. We have taken the energy-integrated intensity of the harmonic, as it would be done in an experiment, over an interval of half the frequency of the driving laser to the left and to the right of the nominal harmonic value.

Supplementary Figure 1 shows the comparison between the helicity-integrated (total intensity) of the harmonics in a trivial and topological insulator, like those presented in Fig.1 of the main manuscript; an observable that does not readily distinguish the trivial and topological phases.

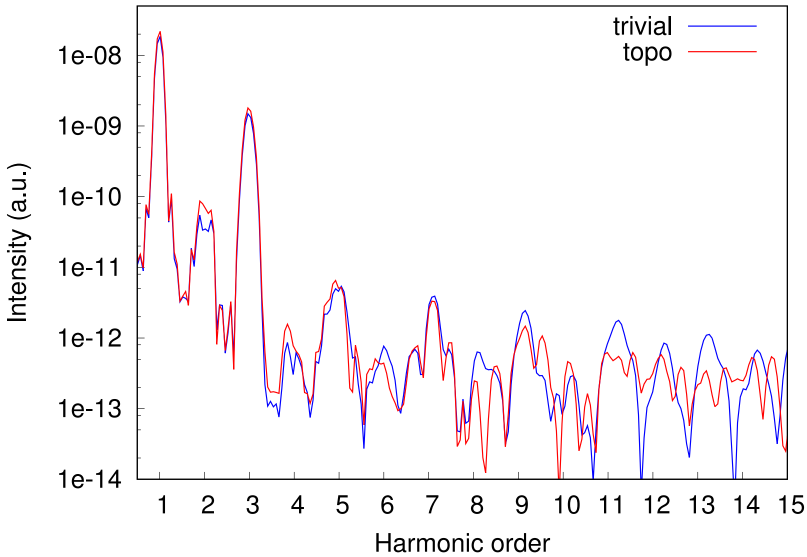

Supplementary Figure 1: **Total intensity of high harmonics in a trivial and topological insulator**. Trivial (blue line) has $M/(3\sqrt{3}t_2) = 1.07$, $\phi = \pi/2$, while topological (red line) has $M/(3\sqrt{3}t_2) = 0.93$, $\phi = \pi/2$.

Supplementary Figure 2 shows the helicity of the odd high harmonics H5 and H7, which were not shown in the main text due to limited space. The parabolic features in H5 not following the helicity change upon the phase transition, will be addressed in Supplementary note 3.

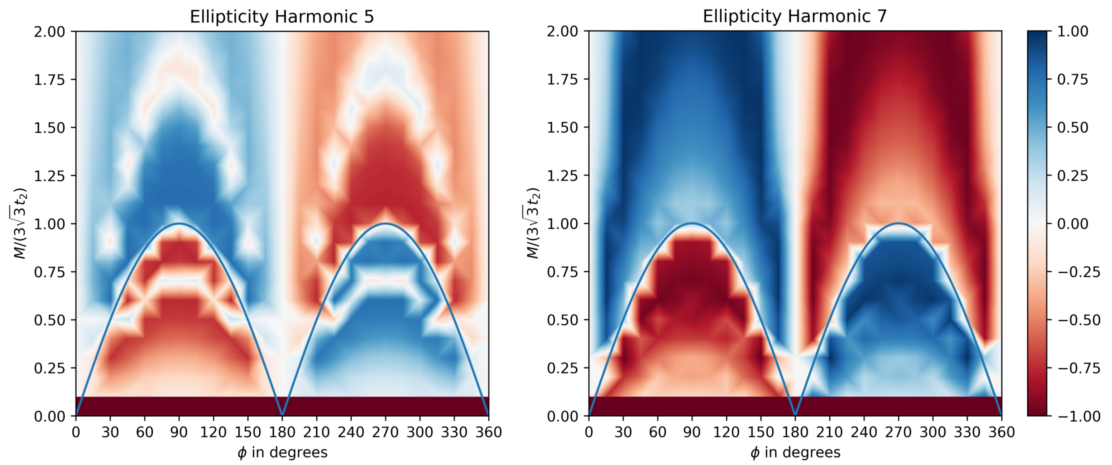

Supplementary Figure 2: **Helicity of harmonics in topological insulators**. Helicity of the fifth (left) and seventh (right) harmonics as a function of the amplitude $M/(3\sqrt{3}t_2)$ and phase ϕ of the second neighbour hopping. The blue line indicates the topological phase transition.

Equation 1 allows us to define an observable,

$$\mathcal{E} = \frac{\mathrm{sgn}(e_{H1}) - \mathrm{sgn}(e_{H3})}{2}, \tag{2}$$

which unambiguously shows if the system is trivial or topological in an all-optical way. This quantity exactly coincides with the Chern number. Supplementary Figure 3 shows this observable for all relevant values of t_2 and ϕ, that accurately reproduces the phase diagram of Chern insulators (Fig.1a in main text).

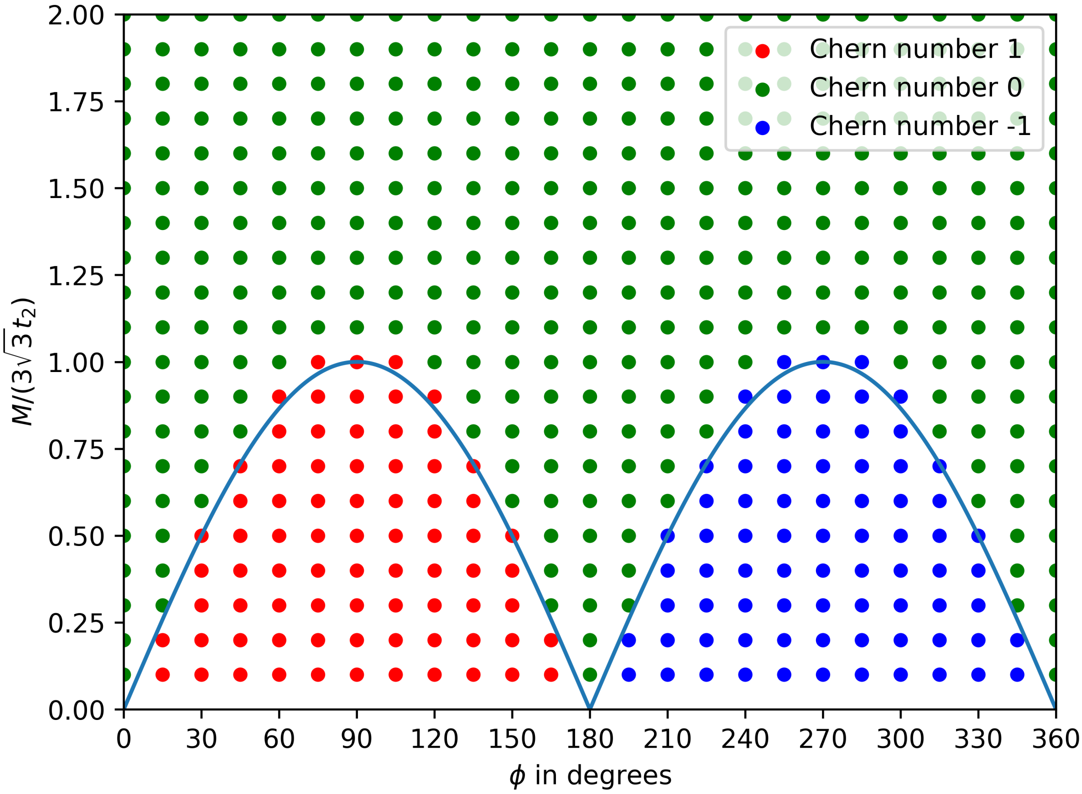

Supplementary Figure 3: **Optical retrieval of the Chern number**. Phase diagram of the Haldane model obtained by using Eq. 2. Each point is a calculation. Green points indicate $\mathcal{E} = 0$, red points $\mathcal{E} = 1$ and blue points $\mathcal{E} = -1$, which coincide with the value of the Chern number. The blue solid line represents the topological phase transition.

We also note that the method to characterize the phase transition is equally valid if the laser were polarized along the x-direction, i.e., along G-M. In Supplementary Fig. 4 we show the helicity-resolved high harmonics in a trivial and topological state generated by a linearly polarized laser along x, which show the same features as those we comment on the manuscript.

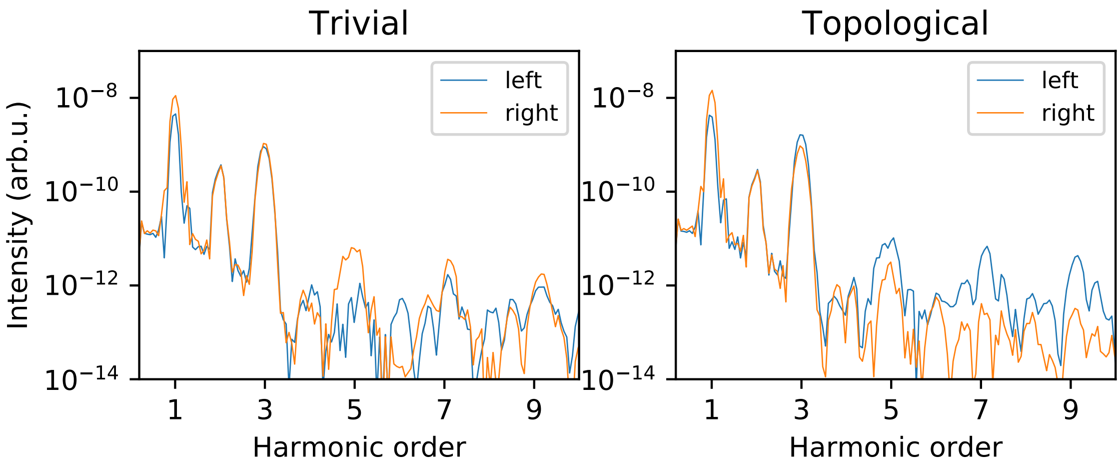

Supplementary Figure 4: **Helicity-resolved HH spectra for linearly polarized driver along x direction**. (a) Trivial phase with $M/(3\sqrt{3}t_2) = 1.1$, $\phi = \pi/2$, and (b) topological phase with $M/(3\sqrt{3}t_2) = 0.9$, $\phi = \pi/2$. Field strength is $F = 4 \times 10^7$ V/cm with 3μm wavelength.

Supplementary note 2

In the manuscript and in Supplementary note 1 we show that the 1st and 3rd harmonic are sufficient to characterize the topological phase transition. In this way, a resonant, modest-intensity field can also be used to distinguish between the two phases. For clarity, in Supplementary Figure 5 we show the harmonics emerging from the trivial and topological phases in: i) a low-frequency, strong field regime, ii) a resonant, moderately strong field regime, where the third harmonic is present.

However, there are benefits in using a strong-field approach versus a one-photon resonant approach. On the one hand, it permits to map out the complete phase diagram of the system. Since the band structure changes dramatically across the phase diagram, using a resonant field would require continuous tuning of the laser frequency from THz to visible/UV. In contrast, the strong-field approach uses the same laser frequency everywhere. On the other hand, broad-band strong field response enables ultrafast temporal resolution: full characterization of spectral phase and amplitude of the harmonic spectrum yields temporal resolution given by the inverse bandwidth of the total spectrum. We use ultrafast time-resolution to study relative time delays in harmonic emission corresponding to the topological and trivial phases.

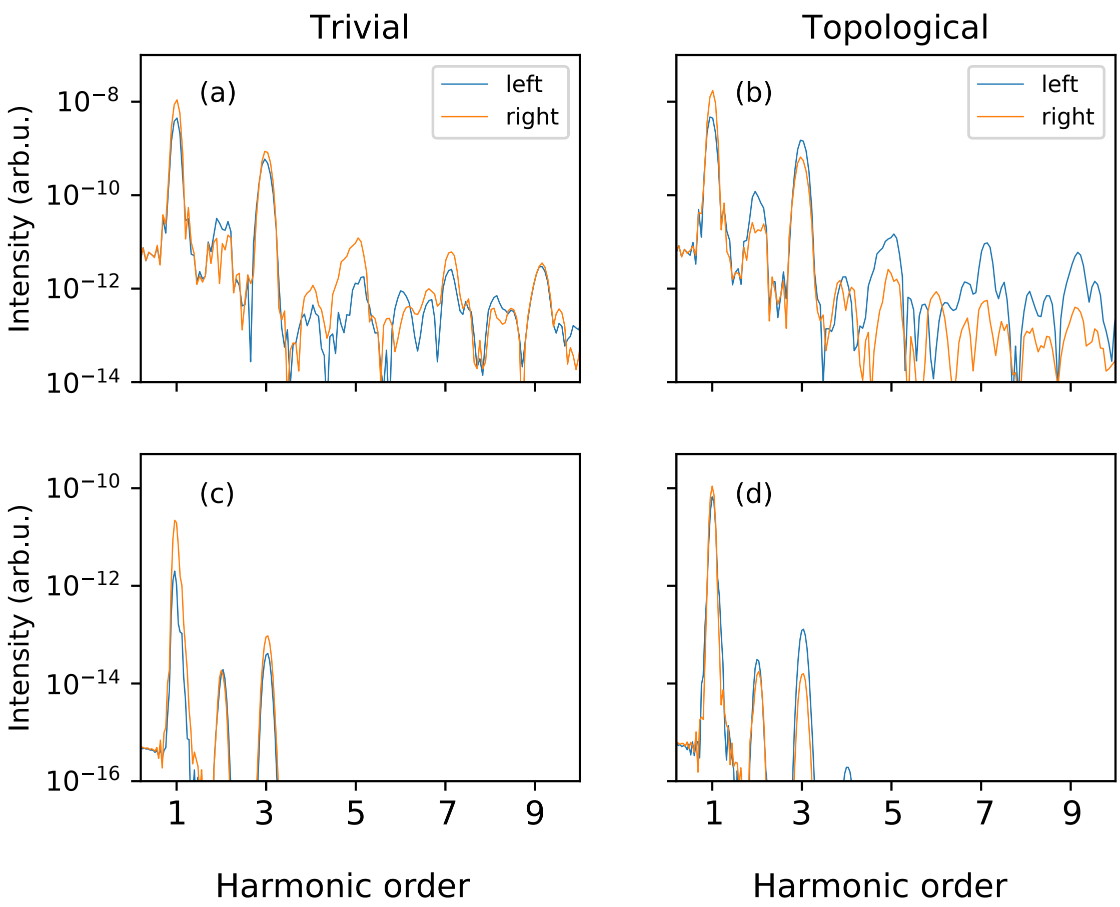

Supplementary Figure 5: **Circularity-resolved high harmonic spectra**. Circularity-resolved high harmonic spectra from a trivial and topological insulator with the same band gap $\Delta = 0.024$ a.u. The driving laser has field strength F and frequency ω of: (a,b) $F = 4 \times 10^7$ V/cm, $\omega = 0.0152$ a.u., (c,d) $F = 4 \times 10^6$ V/cm, $\omega = 0.024$ a.u.

Supplementary note 3

In the main manuscript, we focus on using linearly polarized light and looking at the helicities of the high harmonics to track the topological phase transition. We note, nonetheless, that it is also possible to use elliptical or circularly polarized drivers and get this information from the total harmonic intensity, and not the helicity (i.e. circular dichroism).

In Supplementary Fig. 6 we show calculations for left and right circularly polarized 3μm drivers with a field strength of $F = 4 \times 10^7$ V/cm. Supplementary Fig. 6 shows the total harmonic intensity of the harmonic signal, not the helicities. “Left” and “right” now correspond to two measurements: one for left circularly polarized driver, another for right circularly polarized driver. Since the system has C_{3v} symmetry and the pulse is circular, the high harmonics in the circular field show peaks at 3N+1 and 3N+2 positions, while the 3N harmonics are symmetry forbidden.

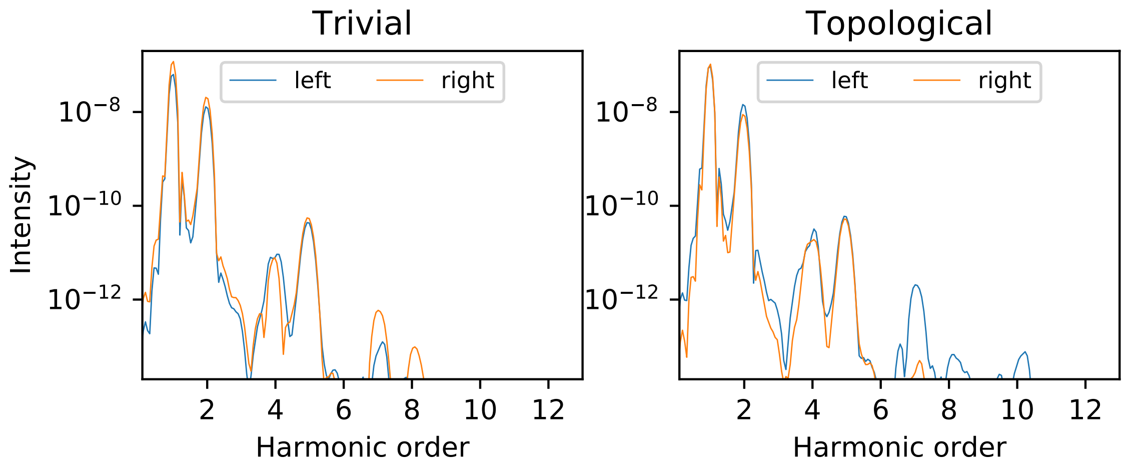

Supplementary Figure 6: **Topological circular dichroism**. Total high harmonic intensity (left panel for trivial, right panel for topological) obtained from two measurements: one using a left circularly polarized driving field (blue) and one using a right circularly polarized driving field (orange). The trivial phase corresponds to a complex second neighbour hopping of $t_2 = t_2^{\mathrm{cr}}/1.1$, $\phi = \pi/2$, the topological phase $t_2 = t_2^{\mathrm{cr}}/0.9$, $\phi = \pi/2$, where $t_2^{\mathrm{cr}} = M/(3\sqrt{3}\sin\phi)$. The field strength is $F = 4 \times 10^7$ V/cm, 3μm driver.

Linearly polarized drivers, nonetheless, provide cleaner diagnostics than circular or elliptical pulses. First, the circularly polarized light itself can induce a topological phase transition, as it does for example in topological Floquet insulators or in the valley Hall effect. The linearly polarized pulse does not introduce such additional bias. This additional bias is clearly seen when using elliptically polarized light. In Supplementary Fig. 7 we show the Haldane topological insulator and a two band model of hexagonal boron nitride (trivial insulator with time reversal symmetry). We clearly see the competing tendencies introduced by the elliptically polarized driving field: the system-induced ellipticity (which reflects its topology) "competes" with the ellipticity that the driving field tends to impose on the emitted harmonics. Second, high harmonics are less intense in circular fields, as can be seen by comparing Supplementary Fig. 6 and Supplementary Fig. 5.

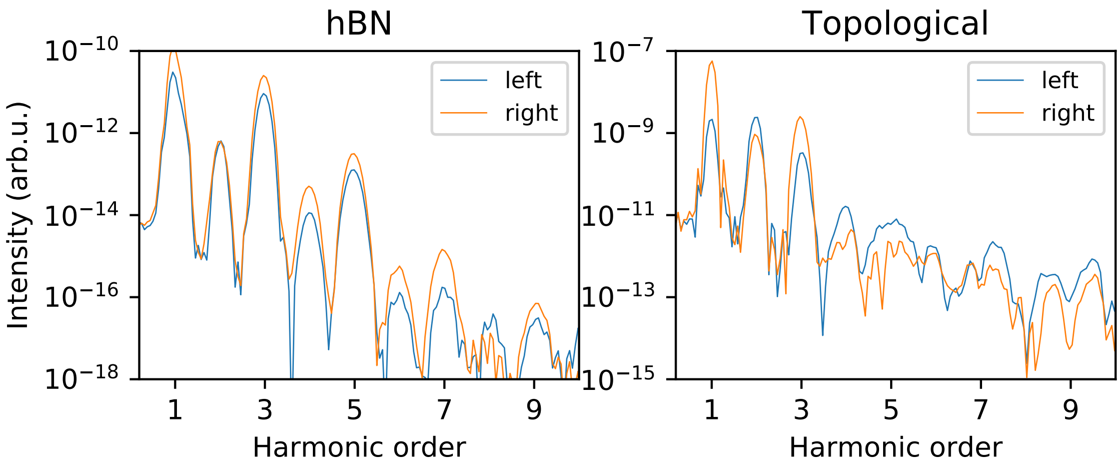

Supplementary Figure 7: **High harmonic spectra for elliptical driver.** High harmonic spectra, resolved in helicity, generated by an elliptically polarized (e=0.3) driver in a two-band model of hexagonal boron nitride (left panel) and the Haldane system ($t_2 = t_2^{\mathrm{cr}}/0.9, \phi = \pi/2$).

Supplementary note 4

In the manuscript we have concentrated mainly on relatively low-order harmonics. The reason is that these harmonics are associated with the area close to the electron injection point near the minimum bandgap. This applies to Brunel, Bloch, and lower recombination-driven harmonics (which are also generated near the injection point). In the region close to the minimum bandgap, the Berry curvature in the trivial phase is strong and has opposite sign for the trivial and topological phases.

However, as we move away from this region, in the trivial phase, the Berry curvature changes sign. This has effect on the electron deflection and makes the analysis less straightforward. Second, in the plateau region of the harmonic spectrum, several recollision trajectories may interfere. Not only these are the long and short trajectories, but also these are trajectories which, due to the spread in the initial electron and hole velocities, recombine from different parts of the Brillouin zone, bringing the properties of the recombination matrix elements directly into the play. This also makes the analysis less straightforward. In the topological phase, where the Berry curvature has the same sign everywhere, the analysis remains relatively straightforward and generally valid for all harmonics irrespective of their physical mechanism and origin in the Brillouin zone.

Supplementary Fig. 8 shows helicity-resolved results across all harmonics, for trivial and topological phases, and for several points in the phase diagram. For topological cases (right column), the dominant helicity is always opposite between the first harmonic and the higher harmonics. For the trivial case (left column), close to the phase transition point (panel a), the recombination harmonics sense the change in the sign of the Berry curvature far from the injection point, leading to the deviation of the results from the straightforward picture obtained for the injection current driven harmonics (Brunel or Bloch). As we change the system parameters away from the phase transition point, the simple picture is restored (panels (c,d)).

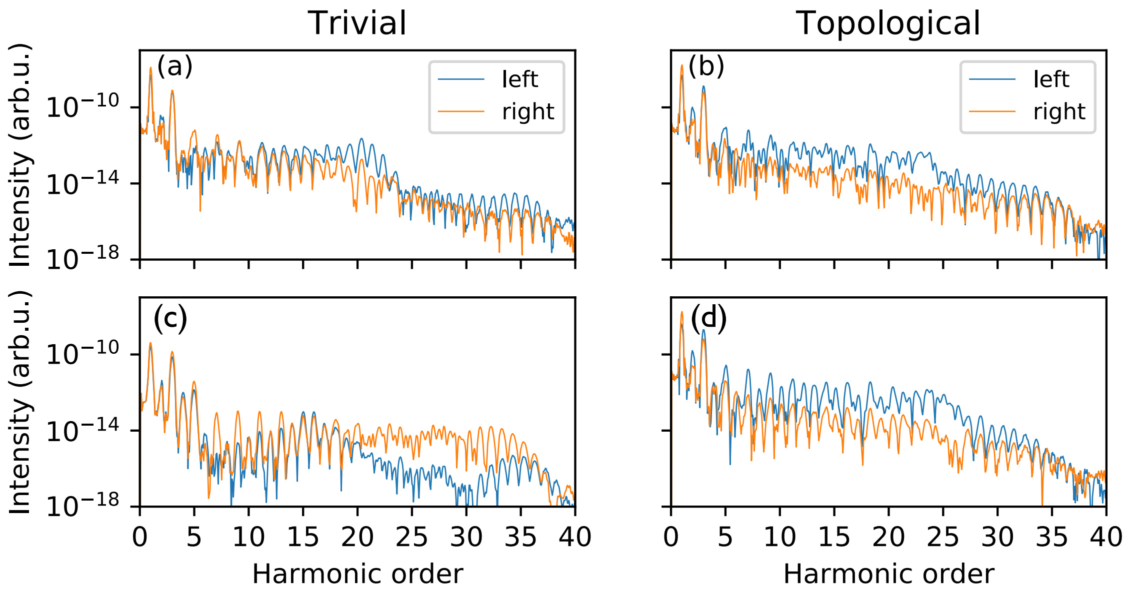

Supplementary Figure 8: **Helicity-resolved high harmonic spectra**. (a) Trivial, $t_2^{\mathrm{cr}}/t_2 = 1.1$, $\phi = 90°$, (b) topological, $t_2^{\mathrm{cr}}/t_2 = 0.9$, $\phi = 90°$, (c) trivial, $t_2^{\mathrm{cr}}/t_2 = 0.8$, $\phi = 165°$, (d) topological, $t_2^{\mathrm{cr}}/t_2 = 0.8$, $\phi = 90°$.

Supplementary Fig. 9 shows the helicity-resolved results across the whole phase diagram. The map of high harmonic helicity provides good map up to H11 and again in the cutoff region starting from H23 all the way to the last harmonic with adequate signal.

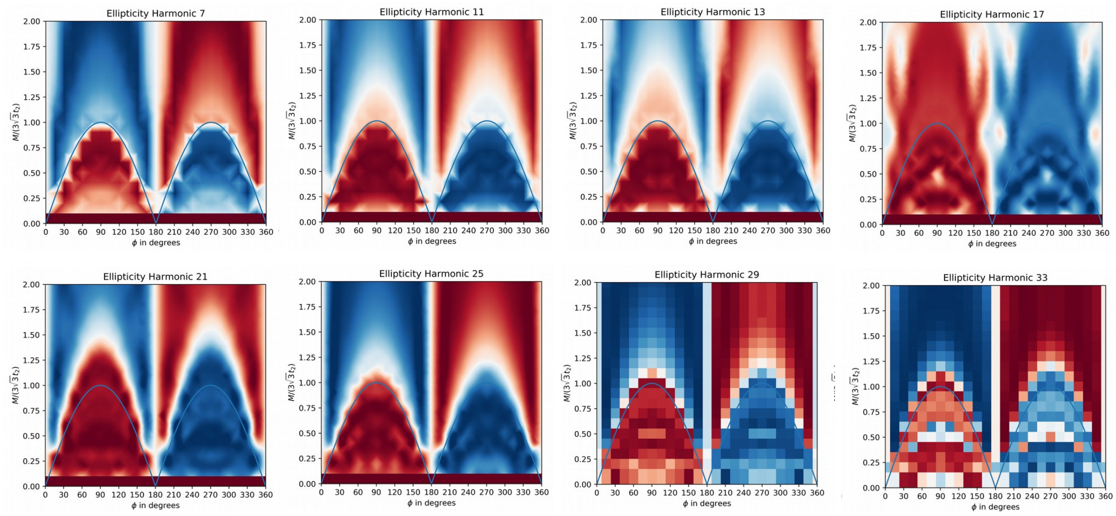

Supplementary Figure 9: **Phase diagram as a function of ellipticity**.Helicity-resolved recombination-driven (inter-band) harmonics across the whole phase diagram. Change in the sign of the Berry curvature away from the injection point in the trivial state of the system affects the harmonic helicity and the simple mapping obtained for the current-driven harmonics. Note that very low intensity of the highest harmonics and their complex spectral shape affects accurate retrieval of their helicity.

Supplementary note 5

Due to limited space, Fig.1b in the main text only shows the band structures for a minimum band gap of $E_{bg} = 0.32$ eV. In Supplementary Figures 10-13 (left panels) we show the band structures of the trivial and topological systems for minimum band gaps of $E_{bg} = 0.22, 0.44, 0.65$ eV. The band structures in both phases are essentially the same. As we move away from the phase transition, and the band gap increases,the band structures of the trivial and topological insulators will start to differ close to the minimum band gap (see Supplementary Figure 14).

Figure 3a,b of the main text show the time map of harmonic 3 for the band structures corresponding to $E_{bg} = 0.32$ eV, for both the trivial and topological systems. In the direction along the laser polarization, the plots for trivial and topological phases are essentially on top, but they show a clear positive/negative asymmetry in the orthogonal direction, as discussed in the main text. In Supplementary Figures 10-13 (center and right panels) we explicitly show that this is a common feature for other harmonics and other band structures.

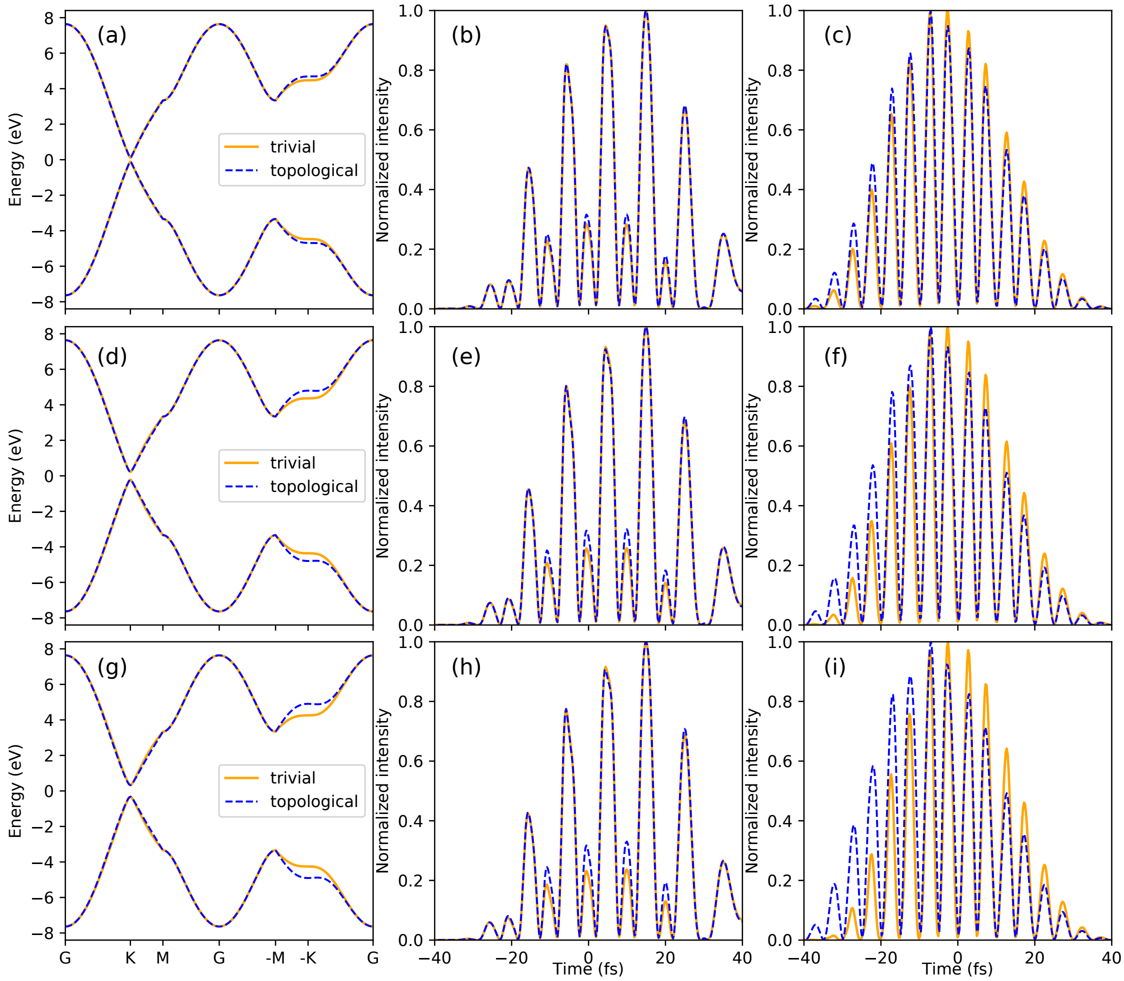

Supplementary Figure 10: **Band structure and time maps for H1**. Left panels: band structure of trivial and topological systems with increasing band gap E_{bg}. From top to bottom: (a) E_{bg} = 0.22, (d) E_{bg} = 0.44, (g) E_{bg} = 0.65 eV. Time map of the emission of H1 in the direction parallel (central panels) and orthogonal (right panels) to the laser polarization, for the band structure on the same row. In all panels, the trivial phase is indicated in solid orange and the topological phase in dashed blue. The driving pulse is centered at 0.

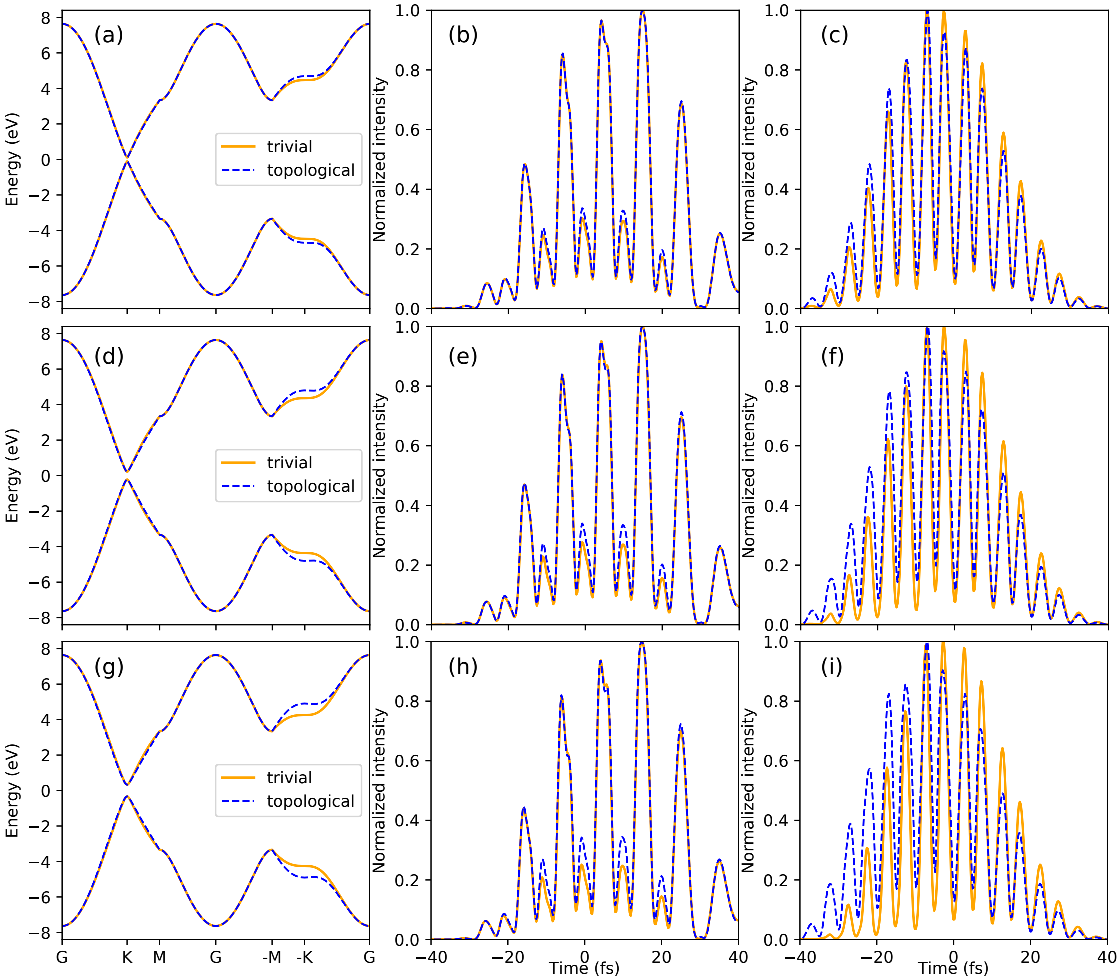

Supplementary Figure 11: **Band structure and time maps for H3**. Same as Supplementary Figure 10 but for harmonic 3.

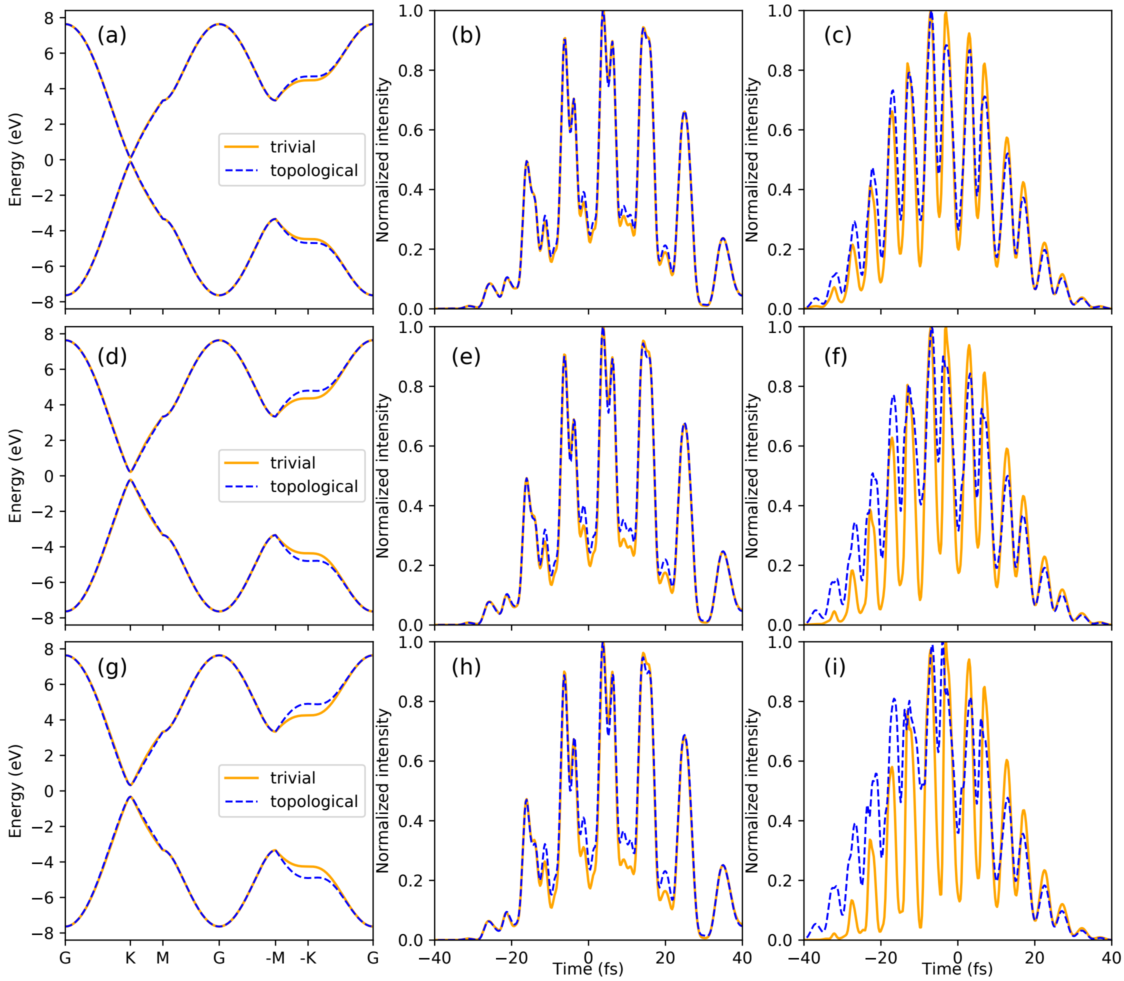

Supplementary Figure 12: **Band structure and time maps for H5**.Same as Supplementary Figure 10 but for harmonic 5.

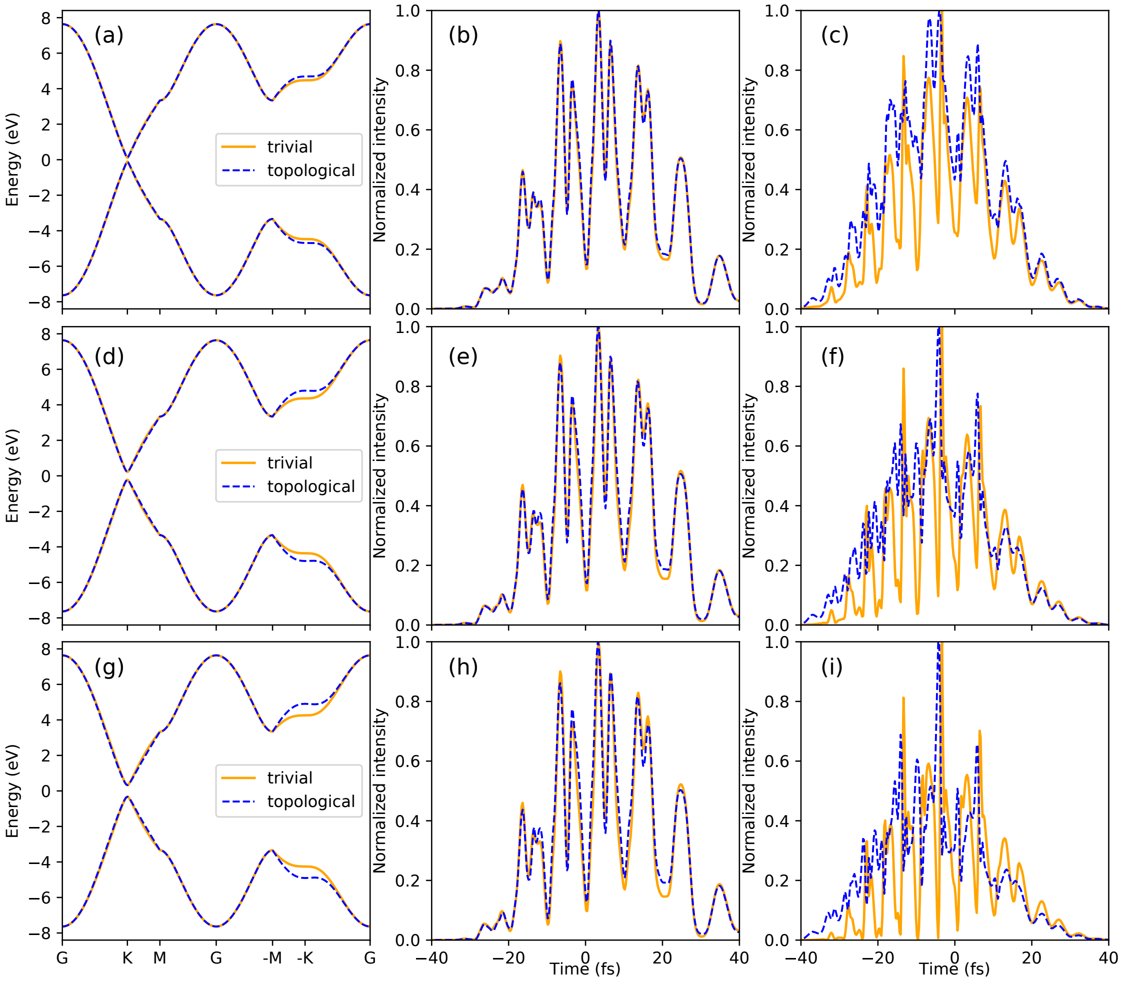

Supplementary Figure 13: **Band structure and time maps for H7**. Same as Supplementary Figure 10 but for harmonic 7.

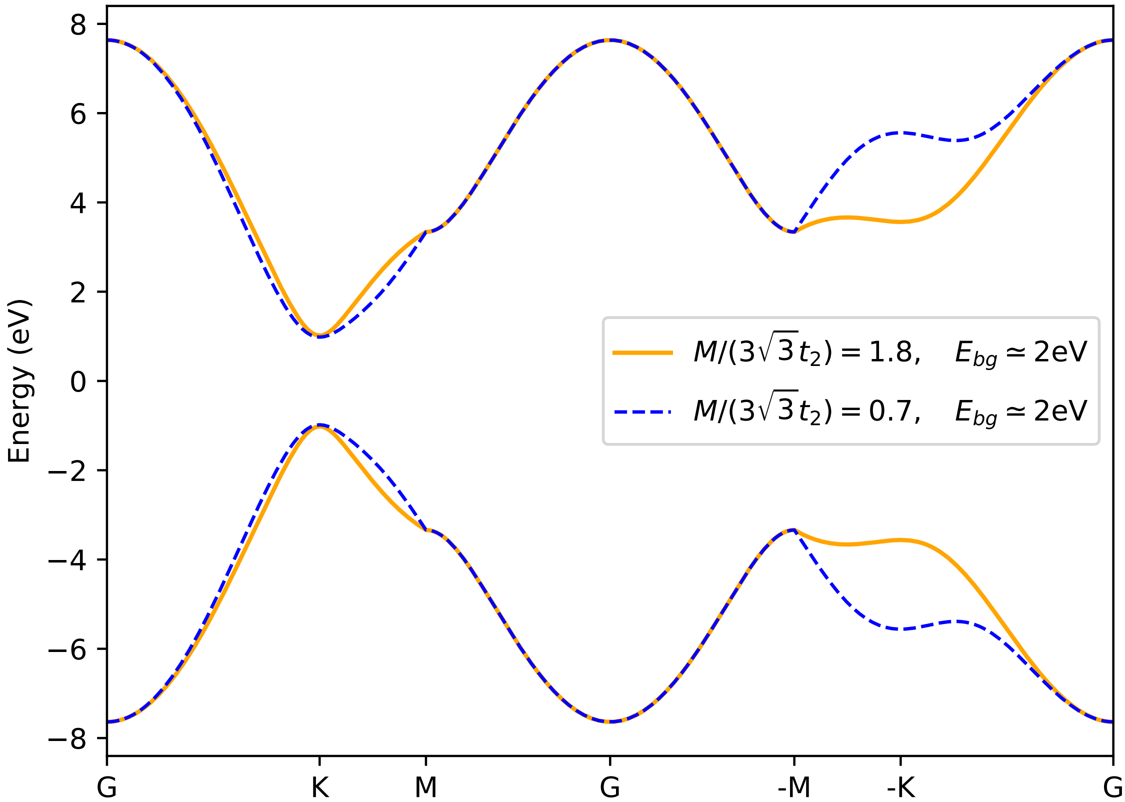

Supplementary Figure 14: **Band structures far from phase transition**. Trivial (solid orange) and topological (dashed blue) phases for a band gap of approximately 2 eV. Far from the phase transition, trivial and topological systems will have different band structures close to the minimum band gap.

Supplementary note 6

In the main text, we have stated that the topological nature of the density manifests in observables. Let us write the momentum-resolved electron density in the conduction band $\rho_{cc}(\mathbf{k}, t)$ as

$$\rho_{cc}(\mathbf{k}, t) = \rho_{cc}^{(0)}(\mathbf{k}, t; \Omega = 0) + \Delta\rho_{cc}(k, t; \Omega) \simeq \rho_{cc}^{(0)}(\mathbf{k}, t) + \Omega(\mathbf{k})\frac{\partial \rho_{cc}}{\partial \Omega}|_{\Omega=0}(k, t), \quad (3)$$

where $\rho_{cc}^{(0)}(\mathbf{k}, t)$ is the Berry curvature-independent injected density, and the second term is the correction, linear in the Berry curvature Ω in the first order. While this additional term is small (see Fig. 1c,d of manuscript), its contribution to the anomalous current is quadratic in Ω and does not change sign during the phase transition, in contrast to the main contribution. If the main contribution to the harmonic emission, associated with $\rho_{cc}^{(0)}(\mathbf{k}, t)$, is suppressed for a particular harmonic, the additional contribution associated with $\Delta\rho$ could become visible and the helicity of the harmonic should flip. We observe such flips in the helicity map of harmonic 5 (see the two parabolas centred at $M/(3\sqrt{3}t_2) = 0.7$ and 1.75, in Supplementary Figure 2). This is accompanied by a sudden spectral phase jump in the harmonic line, reflecting destructive interference in the main contribution to the harmonic emission.

Supplementary Figure 15 shows this sudden phase changes as an observable (with units of time):

$$\text{time shift}(N) = \frac{\int_{(N-0.5)\omega_L}^{(N+0.5)\omega_L} d\omega\, I(\omega)\, \frac{\partial\varphi(\omega)}{\partial\omega}}{\int_{(N-0.5)\omega_L}^{(N+0.5)\omega_L} I(\omega)\, d\omega}. \tag{4}$$

Here, $I(\omega)$,$\varphi(\omega)$ are the harmonic intensity and phase, respectively, ω_L is the laser frequency and N is the harmonic number. We can clearly observe a sharp change in this observable only near the points of the phase diagram at which the helicity changes ($M/(3\sqrt{3}t_2) = 0.7, 1.7, 1.8$), signalling the destructive interference in $\rho_{cc}^{(0)}$, and the dominance of the topologically-dependent component $\Delta\rho_{cc}$.

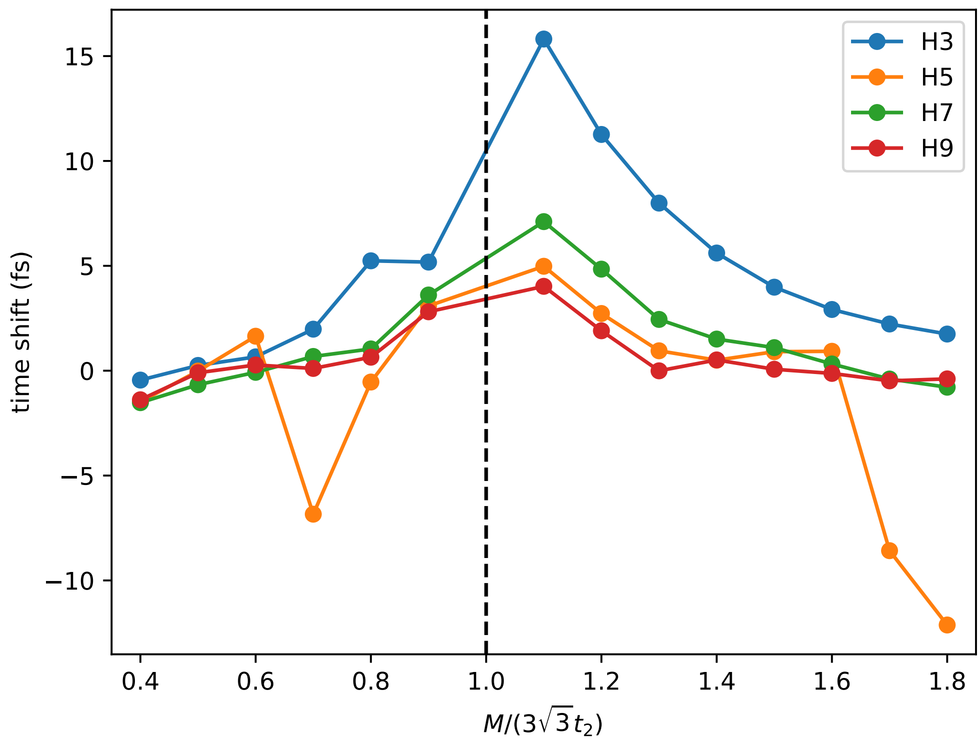

Supplementary Figure 15: **Time shift of harmonics**. The time shift, as defined by Eq. 4, as a function of the amplitude of the second neighbour hopping and fixed $\phi = 90°$, for different harmonics. Sharp changes far from the phase transition at 0.7,1.7 and 1.8, which coincide with helicity changes in the phase diagram (see Supplementary Figure 2), signal a destructive interference in the topologically-independent density contribution to the current.

Supplementary note 7

We have checked that our results are not dependent on the on the dephasing time, on the pulse parameters or on the lattice parameters.

In Supplementary Figure 16 we present calculations performed with no dephasing. We show the helicity of the first nine odd harmonics as a function of the second neighbour hopping amplitude, and the phase diagram, for two fixed values of the second neighbour hopping phase, $\phi = 0°, 90°$. We note that the two points at $(\phi, M/(3\sqrt{3}t_2) = (90°, 0.4), (90°, 0.5)$ correspond to values where $|t_2/t_1| > 1/3$, outside the range of Haldane's model, where the system is metallic.

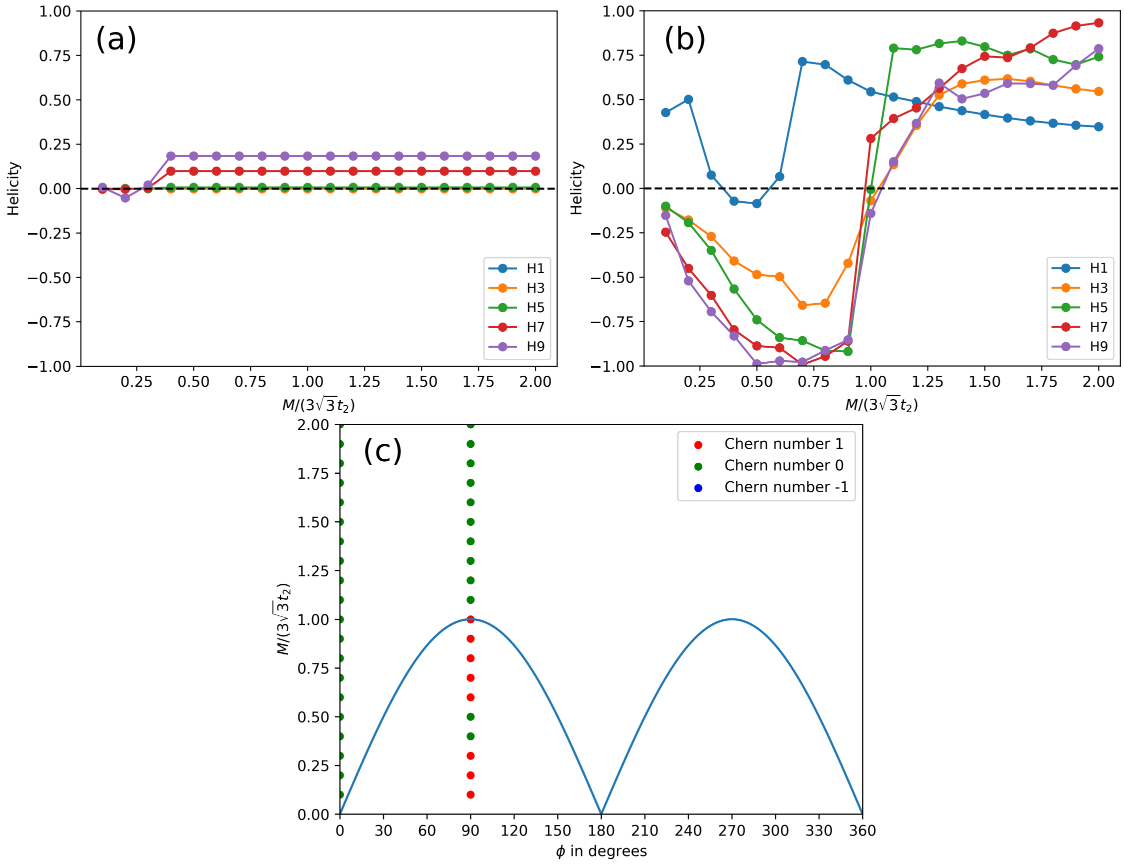

Supplementary Figure 16: **Helicity of harmonics and phase diagram for no dephasing**. Helicity of the first nine odd harmonics as a function of the second neighbour hopping amplitude, for (a) $\phi = 0°$ and (b) $\phi = 90°$. The value $M/(3\sqrt{3}t_2) = 1$ signals the topological phase transition. (c) Optical retrieval of two lines in the phase diagram following the definition in Eq. 2.

Supplementary Figure 17 shows the helicity of the first nine odd harmonics for a fixed $\phi = 90°$ as a function of $M/(3\sqrt{3}t_2)$ values, for different laser intensities, and for a dephasing of 2 fs. We see the same change of helicity in the phase transition for all intensities. Furthermore, the helicity at the point $M/(3\sqrt{3}t_2) = 0.7$ in H5, discussed in supplementary note 3, is dependent on the laser intensity. This is further proof that these points correspond to the zeros of the Bessel function in Eq. 19 of Methods section, that is, where the contribution of $\rho_{cc}^{(0)}$ to the current vanishes.

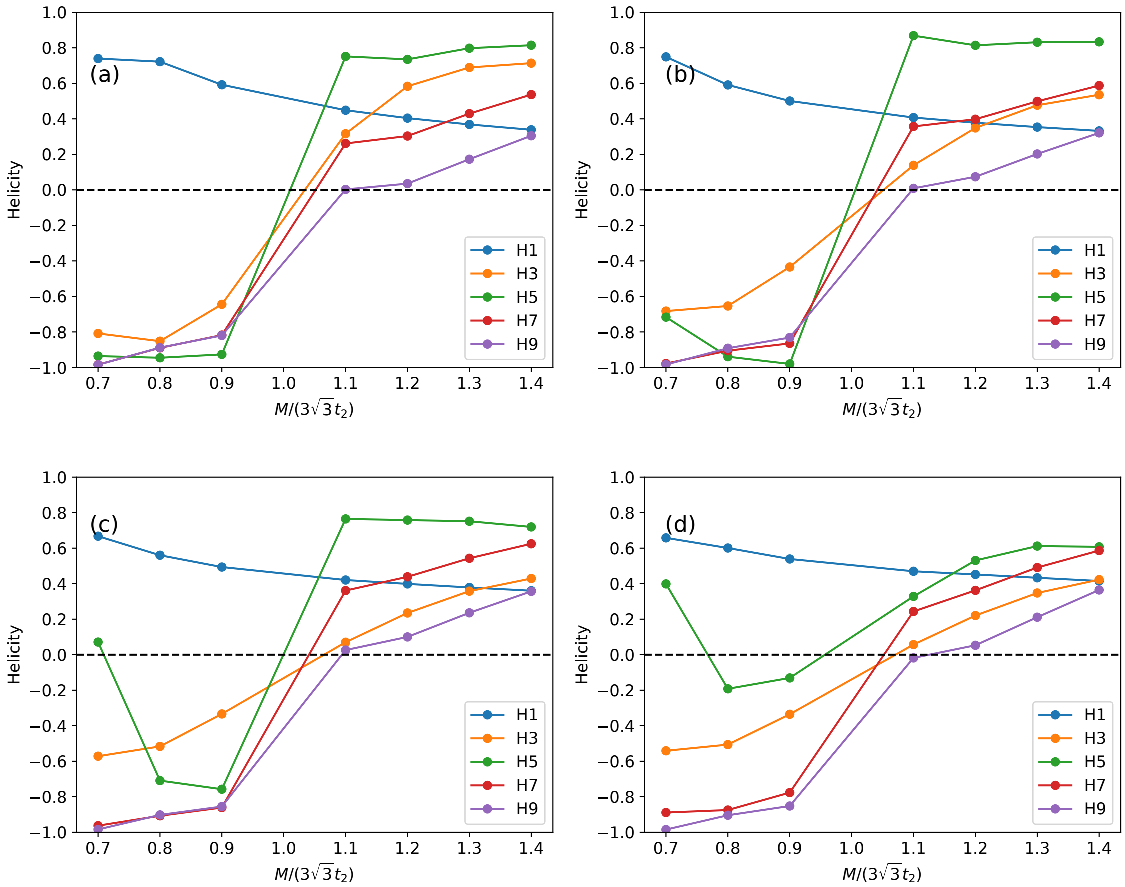

Supplementary Figure 17: **Helicity of harmonics for different laser intensities**. Helicity of the first nine odd harmonics as a function of the second neighbour hopping amplitude, for driving field strengths of (a) E = 2 GV/m, (b) E = 3 GV/m, (c) E = 4 GV/m and (d) E = 0.5 GV/m. The value $M/(3\sqrt{3}t_2) = 1$ signals the topological phase transition.

Supplementary Figure 18 shows the band structure and time map of harmonic 3 of a lattice with slightly different parameters. In this case, we have fixed the first neighbour hopping to $t = 0.1$ a.u., the second neighbour hopping to $t_2 = 0.01$ a.u., and we have calculated two systems: one in a topological phase, with on-site energies $M = \pm 0.9(3\sqrt{3}t_2) = \pm 0.047$ a.u., and one in a trivial phase, with $M = \pm 1.1(3\sqrt{3}t_2) = \pm 0.057$ a.u. The results showing the positive/negative asymmetry in the orthogonal component of the time-frequency map is in line with that obtained earlier with other lattice parameters.

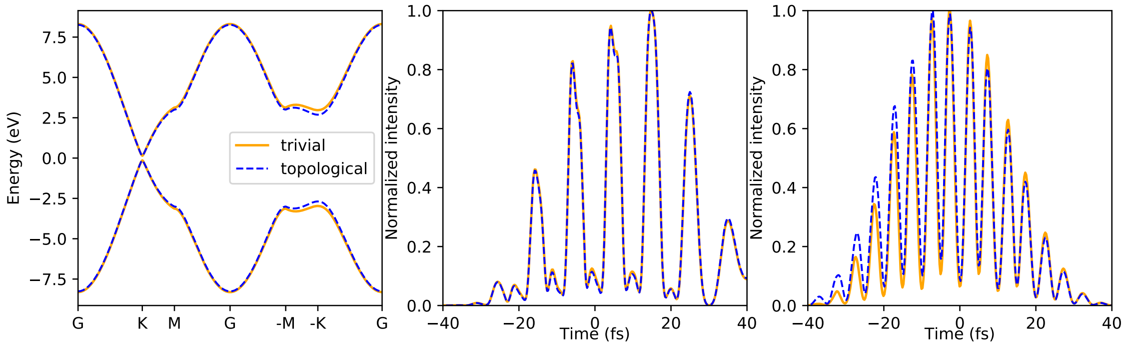

Supplementary Figure 18: **Band structure and time map of H3 for a different set of lattice parameters**. Same as Supplementary Figure 11, but with different lattice parameters (see text for details).

Supplementary note 8

In Supplementary Fig. 19 we show that the intraband component in the direction orthogonal to the laser field can be neglected with respect to the anomalous component, as stated in the main text.

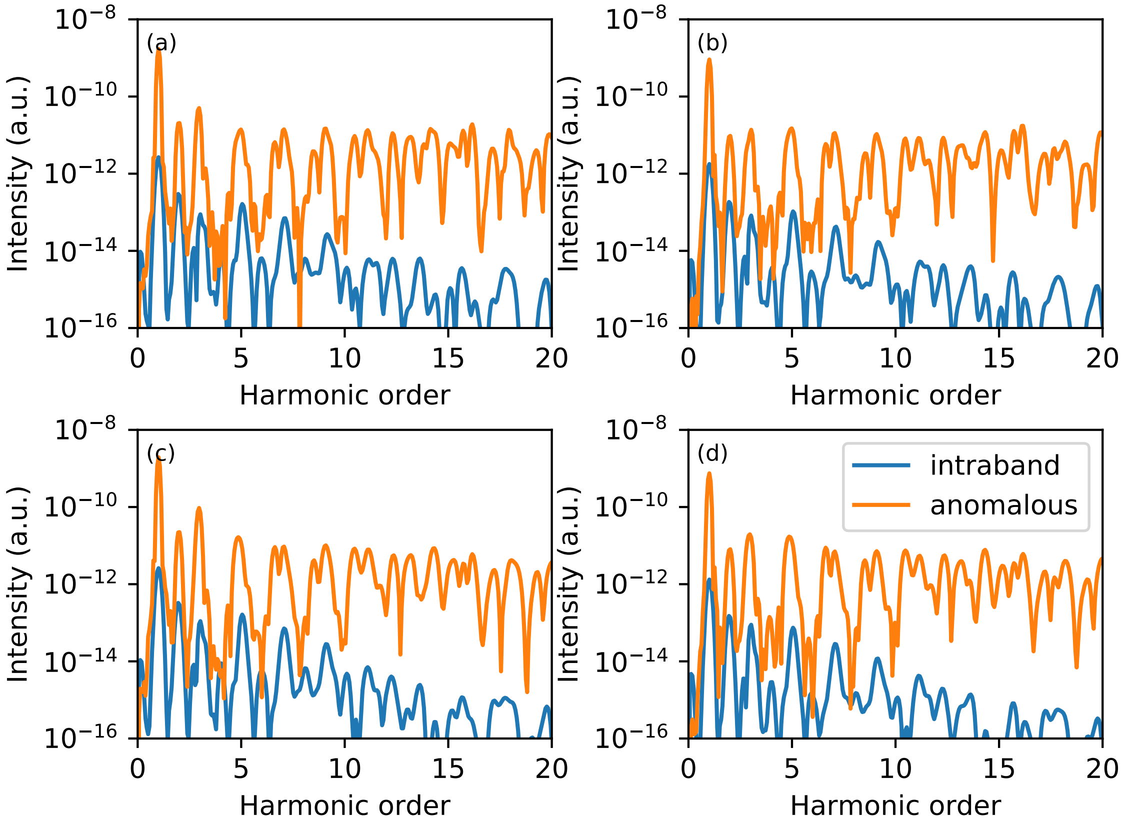

Supplementary Figure 19: **Intraband/anomalous current orthogonal to laser field**. Intraband and anomalous currents in the direction orthogonal to the laser field, for four example systems: (a) topological system with band gap of 0.32 eV, (b) trivial system with band gap of 0.32 eV, (c) topological system with band gap of 0.54 eV, (d) trivial system with band gap of 0.54 eV. Logarithmic scale is used.